Chemical Vapor Deposition of Carbon on Graphite by Methane Pyrolysis

Sreekanth Bammidipati, Gregory D. Stewart, and J. Richard Elliott, Jr.
Chemical Engineering Dept., The University of Akron, Akron, OH 44326

Suleyman A. Gokoglu
NASA Lewis Research Center, Cleveland, OH 44135

Mark J. Purdy
BF Goodrich Aerospace, Inc., Brecksville, OH 44141

Chemical vapor deposition (CVD) of carbon by methane pyrolysis onto a nonporous graphite rod was studied experimentally in a hot-wall, laminar-flow reactor and theoretically by finite-element modeling. Reactor pressure ranged from 10 to 40 torr, control temperature from 1,000 to 1,100°C, and methane was diluted with H_2, Ar, or N_2. The average residence time ranged from 1 to 50 s. A combination of experimental measurement and numerical modeling was used to accurately characterize fluid and thermal fields inside the reactor. Tractable numerical models were developed for the CVD of carbon with gas-phase chemical reaction mechanisms based on accepted kinetic expressions. Simpler mechanisms were reduced from ones based on a more extensive list of intermediate reactions by systematic comparison to experimental data. A simplified but rational model is recommended based on the best fit to experimental data at various flow rates and pressures. The study indicates that axial dispersion plays a significant role and the pressure fall-off effect for rate coefficients of unimolecular decomposition reactions must be taken into account.

Introduction

Aerospace applications of advanced materials represent one of the most promising areas for technological development in aerospace research today. Chemical vapor deposition (CVD) and chemical vapor infiltration (CVI) are widely used processes for the production of these advanced materials. CVI is very similar to CVD but is complicated by pore diffusion resistance and densification gradients. Many protocols for CVI have been suggested (cf., Besmann et al., 1991), but the *isothermal* CVI technique is the most commonly practiced because it is more economical to develop, more versatile for different geometries, and easier to scale up. Despite recent efforts by Starr et al. (1994) for SiC CVI and McCallister and Wolf (1993) for carbon/carbon CVI, quantitative representations of the pyrolysis reactions and transport phenomena involved in CVD/CVI have not yet been sufficiently developed for carbon/carbon CVI to permit complete process optimization. This experimental and theoretical study is designed to elucidate many of the subtle features of the pyrolysis/deposition mechanism by concentrating on the chemistry and transport occurring in the regions outside the substrate (i.e., CVD). The processes involved in infiltration will be reported in the future.

A large number of related studies may be found in the literature. The following representative examples illustrate that most of these studies intended to minimize the impact of temperature and concentration gradients. Neuschutz et al. (1993) heated a narrow throat of the reactor with the expectation that reaction/deposition would only occur within the heated zone. Their substrate was a rod suspended from a microbalance in the throat of the reactor. Makarov and Pechik (1974) fluidized small carbon particles such that their surface to volume ratio was relatively high and bulk-phase transport was minimized. Je and Lee (1984) used a tumbling disk in order to minimize the effects of gradients in the reactor dur-

Correspondence concerning this article should be addressed to J. R. Elliott, Jr.

ing the study of carbon deposition from propane. Kim et al. (1992) studied deposition from aluminum nitride on the walls of tubes with varying diameters to investigate the role of surface to volume ratio. Interpretation of their results relied on the negligibility of axial dispersion. In all the studies except that of Neuschutz et al., the deposition rates were determined by weight measurements before and after the reaction. McAllister and Wolf (1993) have studied infiltration of porous disks and porous rods in a hot wall reactor. They treated fluid, thermal, and concentration gradients by a finite volume model and fit the reaction rate to a simple power-law expression. In the present study, we have designed a streamlined reactor in which all gradients were explicitly treated by finite-element modeling. Instead of trying to minimize the gradients, we simply constrain them to be predictable and study the necessity of accounting for the gradients by comparing the models to each other and to experimental data.

Our experiments were designed to measure the deposition on a nonporous graphite rod from pyrolysis of methane as the sole carbon source. In our systematic model development, we first developed continuous stirred tank reactor (CSTR) models with many explicit reactions in the mechanism in order to explore the sensitivity to the assumed species and narrow the field of prospective kinetic mechanisms. In the CSTR models, the comprehensive studies of Tsang and Hampson (1986) and Baulch et al. (1992) were applied to represent the rates of the fundamental reactions. A two-dimensional (2-D) finite-element model based on a commercial code (FIDAP) was implemented to investigate the magnitude of the temperature, flow, and, more approximately, concentration gradients in the reactor. Boundary conditions for wall and substrate temperatures were obtained by direct measurements in the experimental reactor. For computational efficiency, the gas-phase reaction mechanism applied to the finite-element model was oversimplified relative to the 1-D and CSTR models. Based on the 2-D finite-element model, the reactor was redesigned to eliminate recirculation zones. Recirculation can lead to the formation of undesired species and agglomerates via the free radical reactions that are typical of pyrolysis. The 2-D model indicated the presence of small but significant temperature and concentration gradients in the reactor, which raised doubts about the general applicability of the gradientless CSTR model. On the other hand, the 2-D model had difficulty treating surface reactions and complex reaction mechanisms, although fluid and thermal gradients were treated reliably. Disappearance of some species and evolution of others through multiple reactions at the surface, yielding carbon deposition, led to a number of apparent inconsistencies when the 2-D code was applied to species profiles with chemical reaction. Therefore, the discussion below focuses on results from gradientless and 1-D models. These considerations led us toward a 1-D finite-element model which could easily accommodate a complex reaction mechanism while accurately focusing on the axial gradients. The solutions of the 2-D model for very simple model systems indicated that gradients in the radial direction were much less than those in the axial direction. Furthermore, deposition profiles from the 1-D model were nearly equivalent to the results from the 2-D model for these simple models. Hence, the identification of the most suitable chemical mechanism was based on application of the 1-D model.

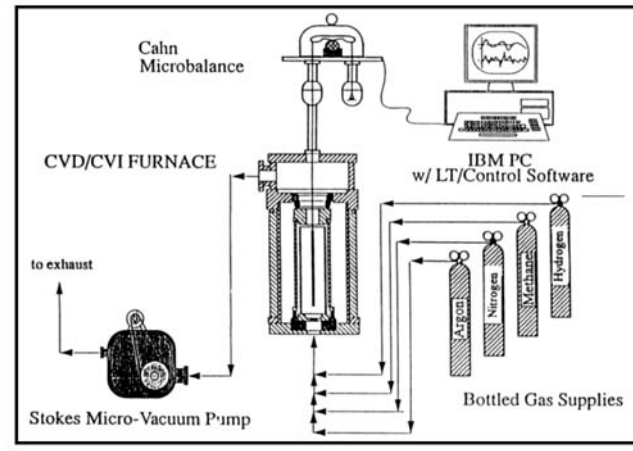

Figure 1. Reactor and peripherals.

The various chemical mechanisms incorporated in the models address the gas-phase and surface reactions of precursor formation and carbon deposition occurring during methane pyrolysis. For the high temperatures and low pressures of interest in this study, we determined that the pressure falloff effects in the unimolecular decomposition reactions were very significant.

Experimental Studies

The experimental low-pressure reactor system used in this work is shown in Figure 1. The gas-flow rates for diluents, nitrogen, argon, and hydrogen, and reactant methane were regulated by separate Brooks Type 580 mass-flow controllers. Mixing was achieved by flowing the gases in a common section of tubing before the reactor inlet. All gases used in this work were laboratory grade with purities listed as follows: H_2 and N_2 were 99.995% min. purity from Akron Welding and Spring Company; and CH_4 was 99.99% min. purity from Matheson.

The gas mixture entered the vertical reactor at room temperature from below and flowed into the reaction zone through a graphite baffle. The baffle was intended to dampen the flow disturbances and result in essentially a flat flow profile. After the baffle, the mixture flowed through a short expansion and preheating section to entering the isothermal reaction zone containing the substrate. Hot gases exited the reactor through a copper packed particle trap located just before the vacuum pump.

In-situ sample weight measurement, setpoints of gas-flow rates, reactor temperature, and pressure were controlled using LT Control by Laboratory Technologies, interfaced to an IBM PC. A strip chart recorder was also used to log reactor setpoint temperature and pressure and weight change of the substrate.

Figure 2 shows details of the furnace used in this experiment. High temperatures in the graphite reaction chamber (102 mm dia. × 241 mm length) are achieved through resistive heating of the outer graphite shell. Owing to the good conductivity of the reaction chamber and uniform heating of the outer reaction chamber walls, an approximately isothermal distribution in the zone surrounding the substrate was achieved. Owing to the isothermal nature of the reaction zone,

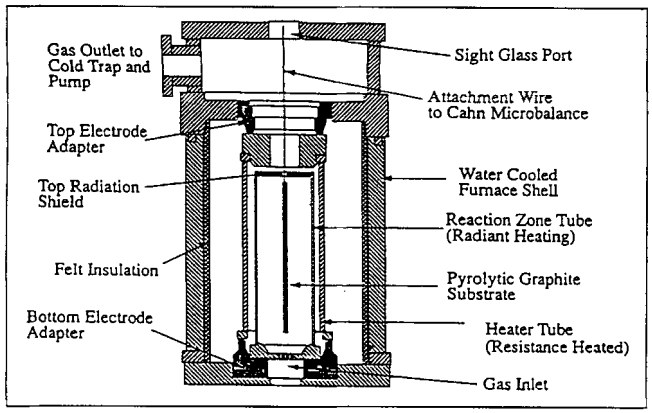

Figure 2. Reactor detail.

radiative effects were deemed negligible in subsequent analysis. The substrate was an ATJ purified graphite cylinder precoated with pyrolytic carbon to fill surface porosity. Its dimensions were 12.7 mm in diameter and 200 mm long. The substrate was hung at the center-most section of the reactor and connected to a Cahn 1,000 microbalance via 0.51-mm-dia. 304 stainless steel wire. This wire was chosen for its small size and ability to resist hydrogen embrittlement for extended experiments at temperatures nearing 1,100°C.

A Stokes vacuum pump and a control valve (MKS Type 253A) located at the exhaust of the reactor were used to control the total pressure in the system to within ± 1 torr at pressure levels of 10 and 40 torr. Before each experiment, the vacuum leak rate was checked and reactor seals adjusted to prevent air leakage. An MKS Baratron Type 122AA pressure transducer and MKS Type 152 controller were used to set and monitor reactor pressure. The reaction zone setpoint temperature was controlled between 1,000 and 1,100°C via an unground Omega Type K thermocouple accurate to ± 3°C. Temperature profiles at the center of the reactor and along the walls were checked using similar temperature probes. No significant carbon deposition was observed on the thermocouple during any of these experiments.

Mathematical Models

In the development of the mathematical models applied in our study, we made a conscious effort to apply readily available software and implement the accepted expressions for the reaction kinetics. Our intention was to show that valuable engineering insights could be gained by adapting the available fundamental technology through the use of a reactor which emulated the industrial practice of interest specifically to the carbon CVI process. The presentation of the mathematical models discusses first the algebraic/differential equations and the software applied to solve them. The pressure fall-off effect and how we characterize it is then discussed. Finally, our approach for reducing prospective mechanisms to simpler, rational models is presented.

Algebraic/differential equations

Among the three different models applied in this study, the isothermal continuous stirred tank reactor (CSTR) model is the simplest ("0-D" model) with perfect mixing assumption, i.e., there is no temperature or concentration gradient in the entire reactor. This model uses an implementation of Broyden's iterative method for solving nonlinear algebraic equations (cf., Press et al., 1992). The 1-D model, based on the COLSYS program of Ascher et al. (1981), solves the coupled second-order boundary value problems that arise from recognizing axial dispersion and temperature gradients. This 1-D model is based on the axial dispersion plug-flow reactor assumption similar to the classical work of Danckwerts (1953). Finally, FIDAP modeling was applied to a 2-D model of heat and momentum transport. FIDAP is a general purpose computer program that uses the finite-element method to simulate many classes of steady-state or transient fluid flows in complex geometries including heat transfer and the species mass transport with chemical reactions. We also attempted to apply the FIDAP code to the multireaction mechanism which we developed, but found that it was extremely difficult to treat such a mechanism. Alternative software for similar reactive flow modeling is available as reviewed by Dombrowski et al. (1993), but there is no indication that other currently available software would perform better than FIDAP. This would appear to be a subject which requires further development by software vendors. The mathematical details of these models can be summarized as follows:

We can express the CSTR equations as

$$\left[1+\frac{t_R}{C_M^0}\Sigma r_i\right]x_i=\left[1+\frac{t_R}{C_M^0}r_i\right] \tag{1}$$

where t_R is the residence time, x_i is the mole fraction of the ith component at the inlet, r_i is the rate of reaction of the ith component, and C_M^0 is the inlet methane concentration.

The rate expressions can be written in the general form

$$r_i=\sum_j R_{ij} \tag{2}$$

where R_{ij} is the net rate of formation of the ith component in the jth reaction. For first-order, second-order, and combination reactions, R_{ij} has the form

$$R_{ij}=\nu_{ij}k_{ij}\left[x_{ij1}^{\nu_{ij1}}x_{ij2}^{\nu_{ij2}}C_M^{0(\nu_{ij1}+\nu_{ij2})}-\frac{x_{ij3}^{\nu_{ij3}}x_{ij4}^{\nu_{ij4}}C_M^{0(\nu_{ij3}+\nu_{ij4})}}{Kc_j}\right] \tag{3}$$

$$Kc_j=\left[10^{a_{Kj}}T^{b_{Kj}}\exp(-c_{Kj}/T)\right] \tag{4}$$

where k_{ij} is the rate constant for the ith component in the jth reaction (discussed in Eq. 11), ν_{ij} is the stoichiometric coefficient of the ith component in the jth reaction, and Kc_j is the concentration based equilibrium constant expressed with parameters a_{Kj}, b_{Kj}, and c_{Kj} given in Table 1. The values in Table 1 were compiled from the references by Tsang and Hampson (1986), Baulch et al. (1992), and Stewart et al. (1989). As shown in Table 2, we have abbreviated the designation of the particular reactor model according to the method for solving the algebraic/differential equations. We refer to the mechanistic models by designations of the form S_{dD}^i, where S identifies the species assumed to be reacting at the surface, i specifies the number of species explicitly recog-

Table 1. Rate Coefficients and Equilibrium Constants for Reactions in Various Mechanisms

Rate Coefficients Reaction	a_∞	b_∞	c_∞	a_o	b_o	c_o	E_i
$CH_4 = 1/2C_2H_2 + 3/2H_2$	17.797	−0.558	52,782	33.339	−3.732	53,596	3,635
$CH_4 = CH_3 + 1/2H_2$	17.87	−0.558	52,782	33.412	−3.732	53,596	3,635
$CH_4 = 1/2C_2H_4 + H_2$	17.797	−0.558	52,782	33.339	−3.732	53,596	3,635
$C_2H_4 = C_2H_2 + H_2$	12.9	0.44	44,670	39.74	−5.973	44,670	2,384
$C_2H_2 = 1/2C_4H_4$	6.217	2.118	18,570	NA	NA	NA	NA

Equilibrium Constants Reaction	a_K	b_K	c_K	a_F	b_F	c_F
$CH_4 = CH_3 + H$	1.163	0.26	52,623	0.45	797	979
$CH_4 = CH_3 + 1/2H_2$	1.71535	0.0175	26,608	0.45	797	979
$H + CH_4 = CH_3 + H_2$	2.25768	−0.225	638			
$CH_4 = 1/2C_2H_2 + 3/2H_2$	18.46	−4.645	29,990	0.45	797	979
$C_2H_6 = 2CH_3$	7.704	−1.236	45,700	0.35		
$C_2H_6 = C_2H_4 + H_2$	6.472	−1.37	17,830	0.35		
$C_2H_4 = C_2H_2 + H_2$	1.60904	0	21,070	0.35		
$C_2H_2 = 1/2C_4H_4$	20	0	0			

nized in the gas-phase reaction mechanism, and d specifies the spatial dimension recognized by the system of differential equations. Thus, the mechanism with the three species, methane, methyl radical (surface reactant), and hydrogen based on the CSTR equations, is designated by M^3_{0D}. As another example, the model based on the 1-D equations for the four species, methane, hydrogen, acetylene (surface reactant), and ethylene, is designated A^4_{1D}. The details of each mechanism are given in Table 2. The surface area for deposition in the CSTR models was assumed to include all the surfaces in the reactor. The total surface area was multiplied by the appropriate sticking coefficient and collision rate to characterize the total rate of surface reaction. The rate of deposition on the substrate was taken to be proportional to the fractional surface area contributed by the substrate.

The 1-D CVD model treats an axisymmetric plug-flow reactor. The equations solved by COLSYS are expressed as

$$C_M^0\left[\frac{d^2x_i}{dz^2} - Pe_{iM}\frac{dx_i}{dz}\right] - Pe_{iM}t_R r_i = 0 \qquad (5)$$

$$Pe_{iM} = UL/\mathfrak{D}_{iM}$$

where t_R is the residence time (L/U), x_i is the mole fraction of the ith component, and r_i is the rate of reaction of the ith component. The form of the rate expression r_i is the same as given for the CSTR model. U is the volume averaged velocity through the reactor, L is the length of the reactor, and $\mathfrak{D}_{iM}$ is the mass diffusivity of the ith component in the mixture. It should be noted that the Peclet number is normally defined in terms of the vessel dispersion number, but for our conditions the dispersion number may be set equal to the mass diffusivity (cf., Levenspiel, 1972). The 1-D model accounted for the temperature variation in accordance with the temperatures measured along the wall of the reactor. The temperature and composition dependence of the diffusion coefficients were included in the model. The equations addressed by FIDAP are the fundamental transport equations at steady state (cf., Bird et al., 1960).

Accounting for the pressure fall-off effect

Generally, the rate coefficient for a gas-phase unimolecular reaction can have a dependence on pressure of the bath gas depending on the temperature and pressure. It involves (1) a high-pressure limit in which the rate coefficient becomes independent of pressure; (2) a low-pressure limit in which the rate coefficient is directly proportional to the pressure; and (3) a fall-off regime which involves a transition from one limit

Table 2. Reactions included in the Various Mechanisms Considered

3 Species, Acetylene depositing, A^3_{dD}
$CH_4 = 0.5C_2H_2 + 1.5H_2$
$C_2H_2 + 2S \rightarrow 2C.S + H_2$

3 Species, Methyl depositing, M^3_{dD}
$CH_4 = CH_3 = 0.5H_2$
$CH_3 + S \rightarrow C.S + 1.5H_2$

4 Species, Acetylene depositing, A^4_{dD}
$CH_4 = 0.5C_2H_4 + H_2$
$C_2H_4 = C_2H_2 + H_2$
$C_2H_2 + 2S \rightarrow 2C.S + H_2$

5 Species Acetylene and Vinylacetylene depositing, AV
$CH_4 = 0.5C_2H_4 + H_2$
$C_2H_4 = C_2H_2 + H_2$
$C_2H_2 = 0.5C_4H_4$
$C_2H_2 + 2S \rightarrow 2C.S + H_2$
$C_4H_4 + 4S \rightarrow 4C.S + 2H_2$

9 Species Acetylene and Vinylacetylene depositing, AV
$CH_4 = CH_3 + H$
$H + CH_4 = CH_3 + H_2$
$C_2H_6 = 2CH_3$
$CH_3 + C_2H_6 = CH_4 + C_2H_5$
$C_2H_5 = C_2H_4 + H$
$C_2H_4 = C_2H_2 + H_2$
$C_2H_2 = 0.5C_4H_4$
$C_2H_2 + 2S \rightarrow 2C.S + H_2$
$C_4H_4 + 4S \rightarrow 4C.S + 2H_2$

to the other. The qualitative features of the pressure falloff effect are most easily explained by a simple Lindemann mechanism. Consider the overall reaction: $A \overset{k_{uni}}{\rightarrow}$ products. The Lindemann mechanism accounts for the existence of two distinct processes in a thermal unimolecular reaction: collision activation/deactivation and reaction.

$$\text{collision activation/deactivation: } A + M \underset{k_0}{\overset{k_0}{\Leftrightarrow}} A^* + M$$

$$\text{reaction: } A^* \overset{k_\infty}{\rightarrow} \text{ products}$$

where M represents the activating/deactivating species provided by the bath gas, and k_{uni} is the unimolecular reaction rate coefficient.

With the steady-state approximation for A^*, the dimensionless rate coefficient is given by

$$\frac{k_{uni}}{k_\infty} = \frac{k_0[M]/k_\infty}{1 + k_0[M]/k_\infty} \tag{10}$$

where k_∞ is effectively the infinite pressure limiting value of k_{uni} and k_0 is effectively the zero pressure limiting value of k_{uni}. $[M]$ represents the total molar density in this notation.

As expected, in the low-pressure limit (as $[M] \rightarrow 0$), k_{uni} is directly proportional to pressure, making the rate effectively second order. In our case the reactant acts predominantly as its own bath gas, because we generally apply pure methane and dilute it only slightly during studies of diluent effects. Thus, the Lindemann description gives the qualitative behavior that is observed experimentally, viz., a unimolecular rate coefficient that becomes independent of pressure at sufficiently high pressures and proportional to bath gas pressures at sufficiently low pressures.

The quantitative accuracy of the rate constant is increased by adopting the closely related form of Baulch et al. (1992)

$$\frac{k'_{uni}}{k_\infty} = \frac{(k_0[M]/k_\infty)}{(1 + k_0[M]/k_\infty)} F_c^X; \qquad X = \frac{1}{1 + \log^2(k_0[M]/k_\infty)} \tag{11}$$

where

$$k_0 = [10^{a_0} T^{b_0} \exp(-c_0/T)]\,\beta_c$$

$$k_\infty = [10^{a_\infty} T^{b_\infty} \exp(-c_\infty/T)]$$

$$F_c = [a_F \exp(-b_F/T) + \exp(-T/c_F)]^{\beta_c^{0.14}}$$

$$\beta_c = (\Sigma x_i \beta_i)$$

$$\beta_i = \frac{E_i}{RT} + \frac{1}{2}\left(\frac{E_i}{RT}\right)^2 \left(1 - \sqrt{1 + 4\frac{RT}{E_i}}\right)$$

where β_i is the correction factor for the collision efficiency and E_i characterizes the collision energy (cf., Stewart et al., 1989). This form considers the microscopic rates of collisional energy transfer and reaction and incorporates the "Center Broadening Factor" F_c, using the principles of RRKM theory (cf., Gilbert, 1989). The temperature dependencies of the rate coefficients are given by modified Arrhenius forms (including the low-pressure correction factor for the collision efficiency) with the parameters specified in Table 1.

To give some idea of the magnitude of the pressure falloff effect, consider the reaction rate for methane decomposition (Unimolecular Reaction: $CH_4 = CH_3 + H$) at 1,000°C and 40 torr. The rate is 40 times lower if calculated with the falloff effect than if calculated with the high-pressure limit. We have incorporated this effect when using kinetic expressions available through the extensive critical compilations of NIST (Tsang and Hampson, 1986) and Baulch et al. (1992). For the very important methane decomposition reaction, we specifically apply the characterization of Stewart et al. (1989), which follows the same form.

Model reduction

Matching the models to the experimental data required the manipulation of several adjustable parameters. The most obvious of these were the sticking coefficients for the surface reactants. The calculated deposition rates were most sensitive to the magnitude of the sticking coefficient since the gas-phase reaction rates were altered only within the stated limits of uncertainty, as discussed below. Nevertheless, the magnitude of the sticking coefficient did not significantly alter the shape of the deposition rate curve (vs. flow rate). The values of the sticking coefficients were determined by minimizing the sum of squared deviations between the model predictions and the experimental results.

The specific values of the gas-phase reaction rate constants also required adjustment in some cases. Since the quoted accuracy of the rate equations given by Baulch et al. is ±300%, we were careful not to exceed this range of reliability. Considering the formation of ethylene from methane, Chen et al. (1975) provided a detailed analysis of the intermediate steps and individual rate constants for each. There were five elementary steps in the mechanism of Chen et al. Because the conditions of our experiments were somewhat narrower than theirs, we were able to simplify their mechanism. For instance, when methane is the primary gas-phase reactant, atomic hydrogen is likely to react rapidly with the readily available methane to form methyl radical and molecular hydrogen, roughly doubling the conversion to methyl radical relative to the simple decomposition reaction. In order to characterize the extent to which the five-step mechanism could be reduced for our conditions, we developed a CSTR model at 1,400 K based on the complete mechanism of Chen et al. and compared it to another mechanism based on a single reaction mechanism consisting of methane decomposition. The methane decomposition rate was multiplied by an "adjustment factor" to account for rapid conversion of the hydrogen atoms to methyl radicals. In this manner we determined the adjustment factor to be 1.7, well within the uncertainty limit of ±300% relative to the value of 2.0 that would be expected from simply doubling the effective rate. It should be noted that this effective rate constant is merely intended as an abbreviation for the overall mechanism of Chen et al., which is convenient for the conditions of interest in this study. We do not suggest this abbreviated mechanism as a global or

semiglobal substitute for the elementary mechanism at any other conditions of interest. For example, if methane was diluted by other hydrocarbons in the feed, then the abbreviated mechanism could lead to significant errors. The abbreviated mechanism has been applied simply to facilitate calculations where we find no deviations between the abbreviated mechanism and the elementary mechanism over the range of conditions studied here. These factors have been incorporated into the rate coefficients given in Table 1. These values were then applied without adjustment in the subsequent modeling efforts. In the three-species models where ethylene was not explicitly recognized, the same rate expression was assumed for the direct conversion of methane to acetylene. Similarly, 4- and 5-species models also use the same rate expression for conversion of methane to ethylene. For conversion of ethylene to acetylene, the basic form given by Tsang and Hampson (p. 1,182) was assumed. This form assumes unimolecular decomposition of ethylene to acetylene and hydrogen. As adjustment factor was also applied to this reaction, but its value was determined by a best fit to the experimental data under consideration which turned out to be 1.5 for our final choice of the A^4_{1D} mechanism. These considerations indicate that there were two adjustable parameters for the four-species models based on acetylene deposition: the sticking coefficient and the adjustment factor for the ethylene to acetylene gas-phase reaction.

Results

Since the rates of reaction are sensitive to temperature, it is important to have a detailed knowledge of temperature profiles in the reactor. Figure 3 shows the smoothed temperature profiles derived from the experimental probes of the temperature at six points along the walls of the reactor with two different setpoint temperatures. The temperatures were controlled reactive to a setpoint probe placed between the reactor walls and the heating elements. The setpoint temperatures were significantly different from the measured temperatures inside the reactor. Similar profiles were also measured at the center of the reactor, suggesting a reasonable approximation of treating the temperature as being relatively constant with respect to radial position. The profiles exhibit a

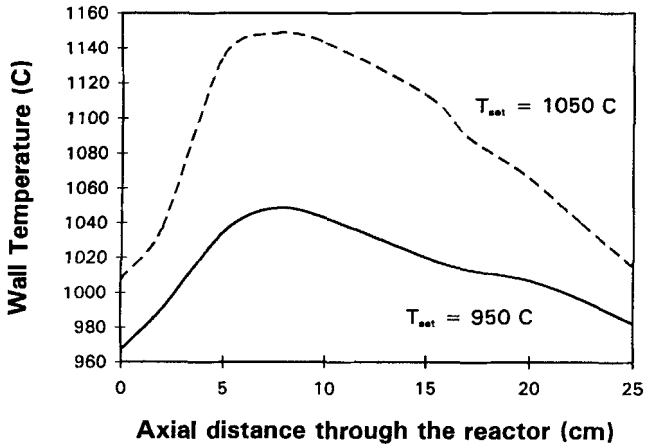

Figure 3. Boundary temperatures in the modified reactor.

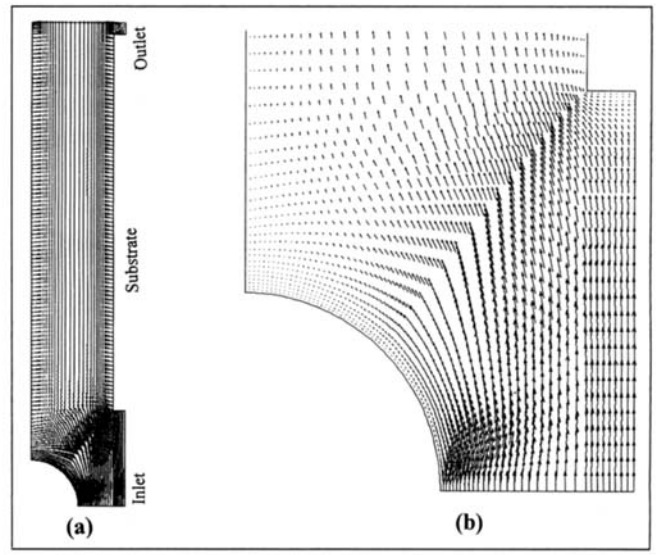

Figure 4. Velocity vectors in the modified reactor.

(a) The overall reactor showing large vectors in the center and short vectors near the walls; (b) enlargement of the vectors in the inlet region.

significant peak in the temperature at about one-third the axial distance through the reactor. Note that the substrate tip begins at about 5 cm through the reactor, so temperatures in the deposition zone were relatively uniform. Preliminary simulations performed with temperatures assumed to be constant at the average value within the deposition zone showed only small differences from results with the detailed temperature profiles, but we applied the detailed profiles in all the results we report here for the 1-D model. For the 0-D model, however, the temperature averaged over the deposition region was used.

Figures 4 and 5 show the velocity and temperature profiles derived from the 2-D model of heat and momentum transport. The vectors in Figure 4 are proportional in size and direction to the velocity at each mesh point. The details in Figure 4a are difficult to read but comparison to the inset in Figure 4b shows that the flow is almost fully developed very shortly after the tip of the substrate. Figure 4 also shows that flows are laminar, and that no recirculations are generated by the presence of the substrate and the nonuniformity of the temperature profiles. It should be noted, however, that recirculation zones are indicated to appear for pressures above 100 torr, even for this streamlined reactor. Figure 5 shows that temperature profiles vary only slightly once beyond the short entrance region. Figure 6 shows the concentration profile for acetylene according to the A^4_{1D} model. In contrast to Figure 5, the gradients in the axial direction are significant throughout the reactor. The concentration of acetylene shows a substantial increase in the axial direction with the decrease near the exit resulting from the temperature decline and a 20% conversion in methane concentration. This gradient indicates that the gas-phase production rate of acetylene exceeds its surface deposition rate at the fit value of the sticking coefficient.

Figure 7 shows that the experimental deposition rates obtained in the modified reactor exhibit a peak relative to flow rate, in qualitative agreement with the findings of Neuschutz

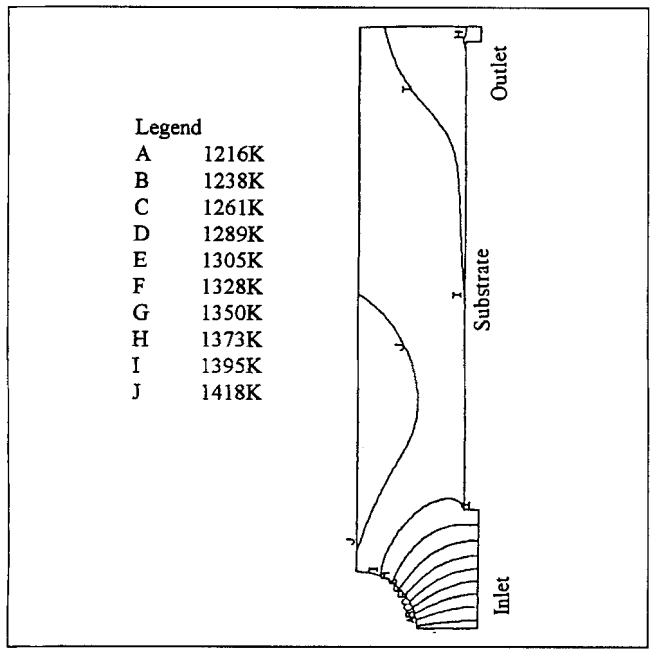

Figure 5. Temperature contours based on the FIDAP simulation.

et al. (1993). The location of the maximum provides significant information with regard to the chemical kinetic mechanism, because it is sensitive to the assumed kinetic model. The trends in this figure and those that follow are plotted with respect to flow rate more conveniently than residence time, because flow rate was the directly measured experimental control variable, although residence times may provide a more general basis for comparison with other data in the literature. If these figures were plotted against residence time, the data for some experiments would be in very different ranges from each other and inhibit a clear understanding of the overall picture. The range of the average residence times can be readily estimated by considering the volume of the reactor 1,969 cm^3, and the flow rate, temperature, and pressure. At 40 torr and 1,415 K, the residence times vary from 3

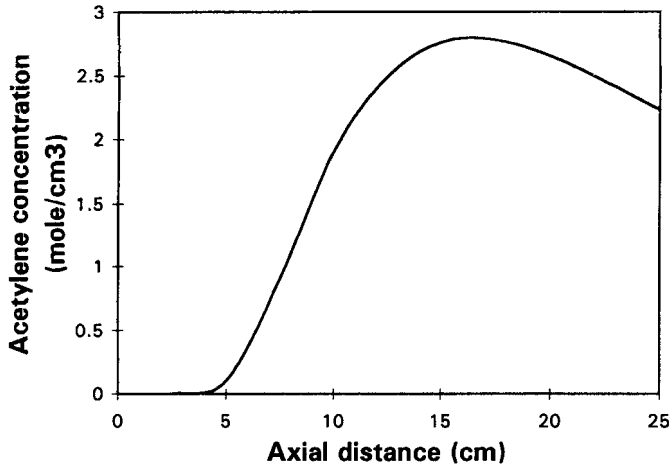

Figure 6. C_2H_2 species profile based on the A^4_{1D} model at 200 std. cm^3/min, 40 torr, and T_{set} = 1,050°C.

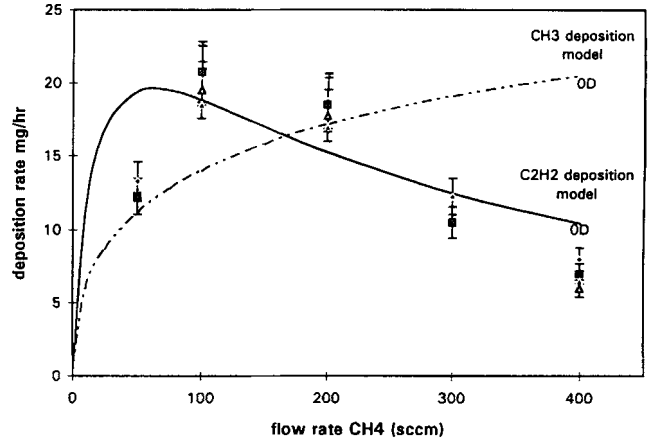

Figure 7. Comparison of the A^3_{0D} and M^3_{0D} models to the experimental data at 40 torr and T_{set} = 1,050°C.

The details of the mechanisms are presented in Tables 1 and 2.

to 26 s. At 10 torr and 1,415 K, the residence times range from 0.8 to 13 s. The shortest time considered was 0.77 s at 1,475 K and 10 torr and 400 sccm. A representative Reynolds number can be estimated in similar fashion based on the reactor diameter and standard correlations for the gas viscosity. Values for the Reynolds number are estimated to range between 0.5 to 20 depending on the gas flow.

Figure 7 also presents our analysis of the difference between assuming methyl radical vs. acetylene as the deposition species. The models considered include the A^3_{0D}, M^3_{0D}, and M^3_{2D} models. All the models in Figure 7 were based on three-species mechanisms in order to maintain a consistent basis for comparison. Although the experimental observations show significant scatter, a mechanism based solely on the deposition of methyl radical could not be justified by our present analysis. In fact, including methyl radical as a surface reactant in our models always impaired agreement with the experimental data, even when the methyl radical was considered along with acetylene for deposition. On the other hand, when acetylene was considered to be the principal surface reactant, agreement with the experimental observations was much improved. This observation is similar to the observations by Frenklach and Wang (1991) in relation to diamond deposition.

Figure 8 shows the comparison among the assumed chemical kinetic mechanisms, each with various levels of simplicity/sophistication and all involving acetylene as the deposition species in a CSTR model. The curves show that there is a significant difference between the A^3_{0D} and the A^4_{0D} models, but a smaller difference between the A^4_{0D} and the AV^5_{0D} models. This suggests that the conversion from acetylene to vinylacetylene does not appear to alter the essential kinetics of this system in a significant way. However, the CSTR models do not provide sufficient guidance in the selection of A^4 or AV^5 as the appropriate reduced mechanism.

Figures 9 and 10 illustrate the experimental and predicted deposition rates with regard to the flow rate at different pressures. Figure 9 clearly shows the improvement that can be attained by applying the 1-D model instead of the 0-D model. Furthermore, the difference between the A^4_{1D} and the AV^5_{1D}

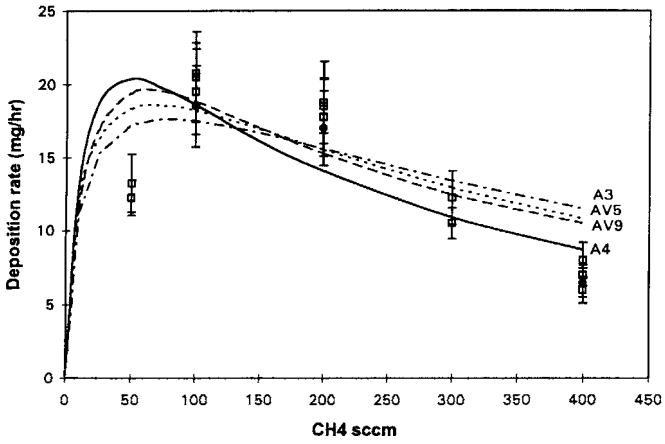

Figure 8. Deposition vs. flow rate for the modified reactor.

Points represent experimental data and curves represent results from the numerical models.

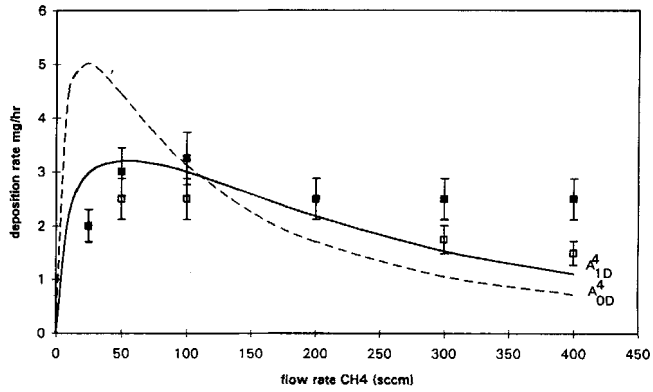

Figure 10. Comparison of the A^4_{1D} and A^4_{0D} models to the experimental data at 10 torr and T_{set} = 1,050°C.

Details of mechanisms are presented in Tables 1 and 2.

models is even less than it was for the 0-D case. The suppression of the deposition rate at low flow rates is the same regardless of the presence of vinyl acetylene in the mechanism. This might be explained by considering the decomposition of methane as rate limiting and noting that both 1-D models treat the decomposition of methane vs. axial distance in much the same manner. Also shown in Figure 9 is the result for the 1-D model in the limit as the diffusion coefficients approach zero. In this limit, the 1-D model becomes equivalent to a nondisperse plug-flow reactor (pfr) so we refer to this model as the A^4_{pfr} model. The A^4_{1D} model (which includes dispersion) gives a result which is intermediate between the A^4_{pfr} model (no dispersion) and the A^4_{0D} model (complete dispersion). Comparison of various models shows that A^4_{1D} reasonably provides accurate agreement with experimental data at both 40 torr and 10 torr, albeit the large error bars in the experimental measurements. Based on these results, there would seem to be little advantage offered by incorporating more complex mechanisms.

Figure 11 summarizes our results at different temperatures and pressures while holding the flow rate constant at 400 std. cm^3/min (sccm). The trends are qualitatively correct. The values of the sticking coefficient shown in Table 3 indicate that the sticking coefficients are not only temperature-dependent, but also pressure-dependent. The trend of increasing values of the sticking coefficient with decreasing pressure (as listed in Table 3) has been observed in other applications of CVD: for example, Blanquet and Gokoglu (1993) in silane deposition. Their explanation is that the surface coverage may become smaller and the active surface sites may become more available for reaction as the pressure is dropped. Therefore, a higher percentage of surface collisions result in surface reaction at lower pressures, i.e., the efficiency of surface reactions increases. It should be noted, however, that the overall rate, which is proportional to the product of surface reaction efficiency and the pressure of the reactive species, does decrease with decreasing pressure because the total number of collisions decreases. The magnitudes of the sticking coefficients are difficult to compare to literature values because previous experiments have not treated deposition on carbon. Allendorf and Kee (1991) have summarized the literature with regard to deposition on silicon surfaces, however. They list a value of 0.02–0.03 for acetylene deposition on silicon at ultrahigh vacuum, significantly higher than our values for depo-

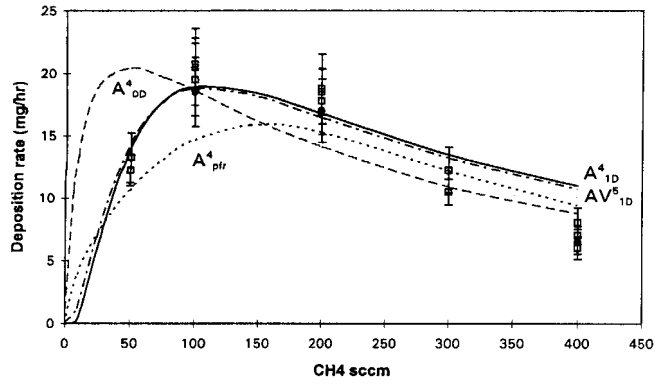

Figure 9. Comparison of the various models to the experimental data at 40 torr and T_{set} = 1,050°C.

Details of the mechanisms are presented in Tables 1 and 2.

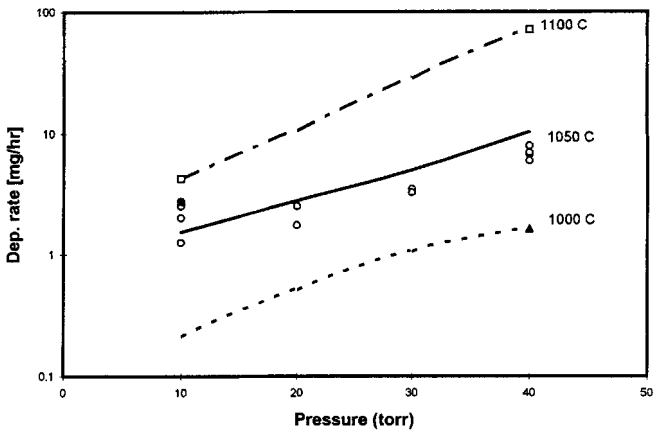

Figure 11. Effects of temperature and pressure on deposition rate at a flow rate of 400 std. cm^3/min.

Table 3. Sticking Coefficients at Temperatures and Pressures of Interest

For Surface Reactions

$k_s = \gamma\sqrt{\frac{RT}{2\pi M_i}}$ where γ is the sticking coefficient for the deposition species

Sticking Coefficients at T_{set} = 1,050°C, 40 torr

Model	Species	γ (10^6)	Species	γ (10^6)
A^3_{0D}	C_2H_2	7		
M^3_{0D}	CH_3	150		
A^4_{0D}	C_2H_2	7		
AV^5_{0D}	C_2H_2	8	C_4H_4	2
AV^9_{0D}	C_2H_2	10	C_4H_4	2
AV^5_{1D}	C_2H_2	8	C_4H_4	5.5
A^4_{1D} p-indp	C_2H_2	0.7		
A^4_{pfr}	C_2H_2	50		

A^4_{1D} *Model* Optimal Values of C_2H_2 Sticking Coefficient γ (10^6)

	Pressure (torr)			
T_{set} (°C)	40	30	20	10
1,100	20			40
1,050	4	16	32	48
1,000	2			

sition on carbon but at different conditions. Also listed in Table 3 for completeness are the values applied for the other models in our study. These range from $0.7(10^{-6})$ to $50(10^{-6})$ depending on the model applied. The low value of $0.7(10^{-6})$ results from the pressure-independent model as a compensating factor for the overestimation of the gaseous rates when the pressure-independent assumption is applied. Similarly, the high value of $50(10^{-6})$ results from the nondisperse plug-flow reactor as a compensating factor for the inaccuracies of that model.

Figure 12 illustrates the effect of diluents in the feed stream on the deposition rate. The total flow rate is fixed at 400 std. cm^3/min in all cases. If the sticking coefficient is assumed to be unchanged by the presence of diluent, the A^4_{1D} model predicts that the deposition rate is only very weakly dependent on the type of dilute (hydrogen, argon, or nitrogen). It should be noted that the gas-phase chemistry is treated in detail by these models. The effects of the bath gas on the unimolecular rate coefficients are included in the models as well as the effects of hydrogen participating throughout the pyrolysis mechanisms. This indicates that neither the bath gas effect

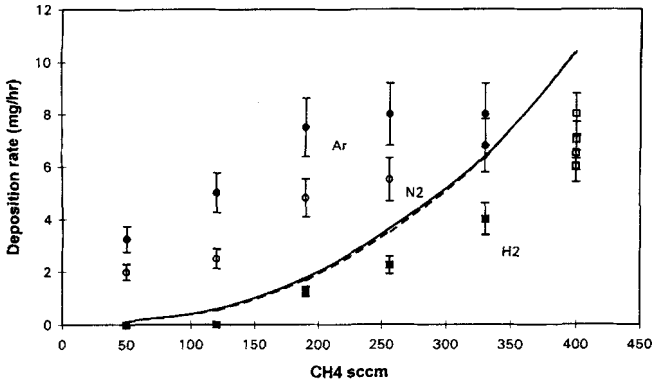

Figure 12. Effect of diluent on the deposition rate.

Total flow rate is 400 std. cm^3/min in all cases; the pressure and temperature are 40 torr and T_{set} = 1,050°C.

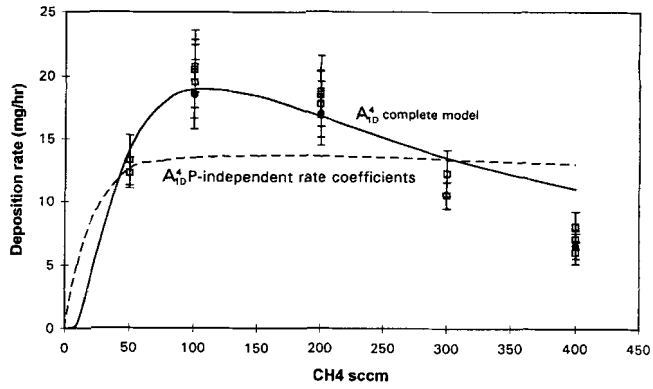

Figure 13. Effect of the pressure dependence of the rate coefficients.

nor the hydrogen-driven reverse reactions affect the deposition rate significantly. If they were important, the model would reflect these differences. In contrast, the experimental deposition rates show that the magnitude of deposition rate suppression depends on the type of diluent. For example, while the presence of argon suppresses the deposition rate in direct proportion to the partial pressure decrease of methane, the data series involving hydrogen as diluent is systematically lower than the other two. For methane flow rates lower than about 150 std. cm^3/min, we observe no deposition in the presence of hydrogen. Hydrogen hindrance effects have been previously noted in other deposition studies (e.g., Hill and Norman, 1975; Comfort and Reif, 1989). This effect may, in fact, be closely related to the decrease in sticking coefficient at higher pressures as discussed in the analysis of Figure 11, i.e., the active surface sites may be covered by adsorbed hydrogen. Such evidence suggests that the surface reaction mechanisms are likely to be more complex than "lumped" first-order kinetics, as implied by the use of sticking coefficient. The surface mechanism may involve hydrogen and possibly argon or nitrogen. At the limit of 400 std. cm^3/min of pure methane (no diluent), the deposition rate vs. flow rate curves should extrapolate to the same limit. The spread in data at 400 std. cm^3/min, however, can neither support nor refute this limit.

The importance of the pressure falloff effect is illustrated in the Figure 13. We compare the pressure-independent A^4_{1D} model to the pressure-dependent model by minimizing the rms deviations of each model relative to the experimental data. The pressure-independent model is relatively flat, because the gas-phase rates are overestimated by a factor of 40. This is a consequence of the decomposition rate coefficients being overestimated at the matched flow rate, which causes the sticking coefficient to be underestimated for all other flow rates. The inclusion of the pressure falloff effect is thus seen to be critical to the accurate representation of the experimental observations.

Conclusions

The 1-D model with a reduced reaction mechanism involving four species (CH_4, C_2H_4, C_2H_2, and H_2), two gas-phase reactions, and only acetylene as the deposition species (A^4_{1D} model) provides the most practical representation of our current understanding of this system. The application of litera-

ture rate data for the gas-phase reactions and the optimal determination of acetylene sticking coefficient were sufficient to describe our experimental observations. For pure methane as a feed, the optimal value of the sticking coefficient for acetylene increases with increasing temperature and decreasing pressure. The type of diluent (hydrogen, argon, or nitrogen) also seems to affect the value of the sticking coefficient. These observations suggest that the surface reactions have more complex mechanisms than the assumed first-order kinetics. The pressure fall-off effect for unimolecular gas-phase reactions is very significant at the operating conditions of interest and should not be neglected in similar modeling efforts. Similarly, the effect of dispersion is intermediate between perfect mixing and plug flow and must be treated explicitly.

The insight gained in the CVD modeling is very useful for further investigations on the infiltration studies of the porous substrates in the processing of densified matrix composites. We expect, however, that a fibrous substrate may give concentration gradients in the radial direction that necessitate the 2-D model for a more accurate description. Incorporating a complex reaction mechanism with pressure-dependent rates may present several significant challenges to the current generation of commercially available software. These undertakings will be the subject of future research.

Acknowledgments

The authors thank BFGoodrich Aerospace, Brecksville, OH for providing all the experimental facilities. The work was supported by the Ohio Aerospace Institute, BFGoodrich, and The University of Akron. Helpful discussions with J. W. Bozelli are also gratefully acknowledged.

Literature Cited

Allendorf, M. D., and R. J. Kee, "A Model of Silicon Carbide Chemical Vapor Deposition," *J. Electrochem. Soc.*, **138**, 841 (1991).

Ascher, U., J. Christiansen, and R. D. Russell, "Collocation Software for Boundary-Value ODE's ACM," *Trans. on Math. Software*, **7**, 209 (1981).

Baulch, D. L., C. J. Cobos, R. A. Cox, C. Esser, P. Frank, T. Just, J. A. Ker, M. J. Pilling, J. Troe, R. W. Walker, and J. Warnatz, *J. of Phys. and Chem. Ref. Data*, **21**(3), 411 (1992).

Besmann, T. M., B. W. Sheldon, R. A. Lowden, and D. P. Stinton, "Vapor Phase Fabrication and Properties of Continuous-Filament Ceramic Composites," *Sci.*, **253**, 1104 (1991).

Bird, R. B., W. E. Stewart, and J. L. Lightfoot, *Transport Phenomena*, Wiley, New York (1960).

Blanquet, E., and S. A. Gokoglu, "Tractable Chemical Models for CVD of Silicon and Carbon," *J. de Physique IV*, **3**, 43 (1993).

Chen, C.-J., M. H. Back, and R. A. Back, "Thermal Decomposition of Methane. I. Kinetics of the Primary Decomposition to C_2H_6 + H_2," *Can. J. Chem.*, **53**, 3,580 (1975).

Chung, G-Y., and B. J. McCoy, "Modeling of Chemical Vapor Infiltration for Ceramic Composites Reinforced with Layered, Woven Fabrics," *J. Am. Ceram. Soc.*, **74**, 746 (1991).

Comfort, J. H., and R. Reif, "Chemical Vapor Deposition of Epitaxial Silicon from Silane at Low Temperatures. I. Very Low Pressure Deposition," *J. Electrochem. Soc.*, **136**, 2386 (1989).

Danckwerts, P. V., *Chem. Eng. Sci.*, **2**, 1 (1953).

Dombrowski, N., E. A. Foumeny, and A. Riza, "Know the CFD Codes," *Chem. Eng. Prog.*, **89**(9), 46 (1993).

Frenklach, M., and Hai Wang, "Detailed Surface and Gas-Phase Chemical Kinetics of Diamond Deposition," *Phys. Rev. B*, **43**, 1,520 (1991).

Gilbert, R. G., *Theory of Unimolecular and Recombination Reactions*, Bladewell Scientific, Boston (1990).

Hill, J., and K. R. Norman, "Hydrogen Desorption: A Possible Rate Determining Step in Pyrocarbon Formation," *Proc. of the 12th Biennial Conf. on Carbon*, Pittsburgh, PA, p. 225 (1975).

Je, J. H., and J. Y. Lee, "A Study on the Deposition of Pyrolytic Carbons form Hydrocarbons," *Carbon*, **22**, 563 (1984).

Kiefer, J. H., and W. A. Von Drasek, "The Mechanism of Homogeneous Pyrolysis of Acetylene," *Int. J. of Chem. Kinetics*, **22**, 747 (1990).

Kim, H. J., Y. Egashira, and H. Komiyama, "Molecular Size and Its Temperature Dependence of Growth Species in the Chemical Vapor Deposition Process of Aluminum Nitride," *J. Chem. Vapor Dep.*, **1**(7), 20 (1992).

Levenspiel, O., *Chemical Reaction Engineering*, p. 496, Wiley, New York (1972).

Makarov, K. I., and V. K. Pechik, "Kinetics of Methane Pyrolysis Under Conditions of Pyrolytic Carbon Formation," *Carbon*, **12**, 391 (1974).

McCallister, P., and E. E. Wolf, "Simulation of a Multiple Substrate Reactor for Chemical Vapor Infiltration of Pyrolytic Carbon within Carbon-Carbon Composites," *AIChE J.*, **39**, 1196 (1993).

Neuschutz, D., S. Zimdahl, and E. Zimmerman, "Kinetics of Carbon Deposition by CVD from Ethylene-Hydrogen-Argon Mixtures at 1000 to 1100°C and 1 Bar Total Pressure," *Proc. of the 12th International Symposium on CVD*, K.J. Jensen and G. W. Cullen, eds., The Electrochem. Soc. (1993).

Press, W. H., S. A. Teukolsky, W. T. Vetterling, and B. P. Flannery, *Numerical Recipes in Fortran*, Cambridge University Press, New York (1992).

Starr, T., A. Smith, T. Besmann, and Sheldon B. McLaughlin, "Modeling of Chemical Vapor Infiltration for Composite Fabrication," *High Temperature Ceramic Matrix Composites*, R. Naslain, J. Lamon, and D. Doumeingts, eds., European Association for Composite Materials, Bordeaux, France, p. 231 (1994).

Stewart, P. H., G. P. Smith, and D. M. Golden, "The Pressure and Temperature Dependence of Methane Decomposition," *Int. J. of Chem. Kinetics*, **21**, 923 (1989).

Tsang, W., and R. R. Hampson, *J. of Phys. and Chem. Ref. Data*, **15**, (1986).

Manuscript received Sept. 20, 1995, and revision received Apr. 29, 1996.